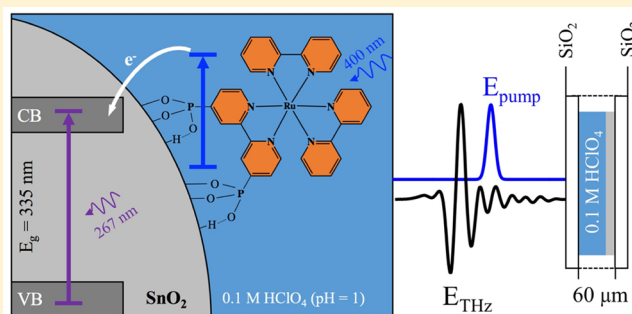


Frequency-Dependent Terahertz Transient Photoconductivity of Mesoporous SnO<sub>2</sub> FilmsKevin P. Regan,<sup>†,‡,§</sup> John R. Swierk,<sup>†,‡,§</sup> Jens Neu,<sup>†</sup> and Charles A. Schmuttenmaer<sup>\*,†,‡,§</sup><sup>†</sup>Department of Chemistry and <sup>‡</sup>Yale Energy Sciences Institute, Yale University, New Haven, Connecticut 06520-8107, United States

## S Supporting Information

**ABSTRACT:** The transient photoconductive properties of tin(IV) oxide (SnO<sub>2</sub>) mesoporous films have been studied by time-resolved terahertz (THz) spectroscopy. We gain insight into carrier dynamics by measuring overall injection and trapping lifetimes using optical pump–THz probe spectroscopy, as well as the frequency-dependent complex conductivity at various pump–probe delay times. It is found that the method of charge generation, either direct above band gap excitation (at 267 nm) or dye-sensitized electron injection (at 400 nm), has a dramatic effect on the overall injection and trapping dynamics of mobile charge carriers on the picosecond to nanosecond time scale. In the presence of aqueous electrolyte, direct band gap excitation of nonsensitized SnO<sub>2</sub> films results in instrument response limited subpicosecond injection lifetimes, while dye-sensitized films require tens of picoseconds for interfacial electron transfer to complete. On the other hand, the rate for trapping of mobile charges is at least 2 orders of magnitude faster in the nonsensitized films compared to the dye-sensitized films, which is likely due to photoinduced charges being more highly concentrated in the nonsensitized films. Finally, we find that the transient photoconductivity deviates from the behavior described by standard conductivity models such as the Drude and Drude–Smith models. This is due to the contribution from a photoinduced change in the permittivity of the SnO<sub>2</sub> films.



## ■ INTRODUCTION

The largest energy source accessible to humanity is the sun; however, harvesting and storing solar energy presents major challenges. One system that potentially addresses this issue is the photoelectrochemical cell (PEC), which in its most common form is a photoelectrolytic cell that utilizes solar energy to split water, generating O<sub>2</sub> at the anode and H<sub>2</sub> at the cathode.<sup>1</sup> Realizing an efficient semiconductor photoanode presents a significant challenge because carrier generation and transport must be coupled to the difficult four-electron, six-atom catalysis of water oxidation. Generation of photoinduced mobile electrons occurs both by direct, above band gap excitation of the semiconductor and via surface-bound dyes that absorb visible light and inject an excited-state electron into the conduction band of the semiconductor. The photoinduced mobile electrons must then be transported through the bulk of the semiconductor material before being shuttled to the cathode to facilitate a reductive reaction. Finally, the electron holes required for water oxidation catalysis can either be transported within the bulk of the material (direct band gap excitation) or hop laterally across the surface via intermolecular hole transfer (dye-sensitized injection).<sup>2,3</sup>

Understanding charge generation due to photoexcitation in a PEC is a crucial step toward harnessing solar energy in the production of fuels (e.g., H<sub>2</sub>, CH<sub>4</sub>, NH<sub>3</sub>, etc.).<sup>4</sup> A major obstacle for PECs is the lifetime of the photoinduced charge

carriers since catalytic reactions occur on a time scale orders of magnitude slower than charge trapping and recombination.<sup>5</sup> It is essential that these transient photoinduced charges are able to move throughout the metal oxide material and survive long enough to initiate the photochemical reaction. The photoelectrochemical behavior and transient spectroscopic properties of photocatalytic metal oxides (e.g., tungsten oxide (WO<sub>3</sub>),<sup>6</sup> titanium dioxide (TiO<sub>2</sub>),<sup>7</sup> and hematite (Fe<sub>2</sub>O<sub>3</sub>)<sup>8</sup>) are well explored in the visible and near-IR absorption regions. Unfortunately, the quantum yields in these materials are low due to their relatively short electron and hole diffusion lengths. Also, the absorption energies are difficult to modify and typically lie in the blue to ultraviolet part of the spectrum.

The absorption onset and fast carrier dynamics can be improved by functionalization with a molecular chromophore.<sup>9,10</sup> Dye-sensitized solar cells<sup>1</sup> utilize a dye-sensitized wide band gap metal oxide and regenerative redox couple to generate photovoltaic power. Water-splitting dye-sensitized photoelectrochemical cells (WS-DSPECs) typically substitute a water oxidation catalyst for the regenerative redox couple to drive photoassisted water splitting.<sup>11</sup> The common choice of metal oxide for these systems is either SnO<sub>2</sub> or TiO<sub>2</sub>.

Received: March 10, 2017

Revised: June 14, 2017

Published: June 21, 2017

While both nonsensitized<sup>7,12–14</sup> and dye-sensitized<sup>9,10,15,16</sup> metal oxides have been studied extensively, there has been only one previous study that characterizes the terahertz (THz) frequency-dependent transient photoconductivity in the presence of an aqueous electrolyte.<sup>13</sup> It should also be noted that there have been studies of the influence of nonpolar solvents on dynamics measured with optical pump–THz probe (OPTP) spectroscopy for their application in DSSCs.<sup>17,18</sup> THz spectroscopy is a noncontact, subpicosecond electrical probe, and measurements are typically made under open-circuit conditions. The lifetime of mobile charge carriers due to photoexcitation can be readily measured using OPTP spectroscopy, which monitors the peak of the THz waveform as a function of pump–probe delay. Our interest lies in understanding the manner in which the mechanism of charge generation affects the ultrafast carrier dynamics in the presence of aqueous electrolyte which more closely mimics a fully functioning photoanode.

In this study, we examine mesoporous tin(IV) oxide (SnO<sub>2</sub>) nanoparticulate ( $d \approx 22\text{--}43$  nm) films as the metal oxide photoanode material for PECs. SnO<sub>2</sub> is an attractive photoanode material for dye-sensitized applications due to its high electron mobility and favorable energy position of the conduction band minimum (CBM) which allows for a wide array of photosensitizers for electron injection.<sup>9</sup> The band gap energy of SnO<sub>2</sub> is 3.7 eV<sup>19</sup> which corresponds to a wavelength of 335 nm (in the UV tail of the AM1.5 solar spectrum), and only 1% of the solar irradiance is above the SnO<sub>2</sub> band gap. Thus, the majority of research has been focused on dye-sensitized systems since they absorb visible light.

We compare lifetimes of carriers in the CB generated via direct above band gap excitation vs carriers generated by dye-sensitized injection. Using OPTP spectroscopy, we find that the method of photoinduced charge generation has a dramatic effect on the overall injection and trapping dynamics of charge carriers on the picosecond to nanosecond time scale ( $\sim 0.3$  to  $\sim 1850$  ps). To further understand the OPTP dynamics, THz transient photoconductivity measurements were made at five optical pump delays,  $t_{\text{pump}}$ . For these, the entire THz waveform is measured at a particular pump delay and then analyzed to obtain the frequency-dependent complex-valued conductivity. Interestingly, the measured conductivity does not follow the Drude–Smith (DS) model as expected.<sup>20</sup> Therefore, we have extended the Drude–Smith model to include a change in the polarizability upon photoexcitation of the sample,  $\Delta\alpha_{\text{photo}}$ , which leads to a change in the real permittivity ( $\Delta\epsilon_{\text{photo}}$ ), which in turn leads to a change in the imaginary conductivity.

## ■ EXPERIMENTAL METHODS

**Preparation of Nonsensitized and Dye-Sensitized SnO<sub>2</sub> Films.** A transparent paste of 22–43 nm diameter SnO<sub>2</sub> nanoparticles was prepared using the method of Ito et al.<sup>21</sup> A more detailed description of sample preparation can be found in our previous work.<sup>15</sup> Briefly, the SnO<sub>2</sub> was doctor bladed onto fused quartz substrates using Scotch Magic Tape as a spacer. The films were dried at 80 °C and then sintered at 470 °C, leading to a thickness of about  $\sim 4$   $\mu\text{m}$ . The photosensitizer, bis(2,2'-bipyridine)(4,4'-diphosphonato-2,2'-bipyridine)-ruthenium(II) bromide, referred to as Ru(II)phos, was prepared by a well-established method.<sup>22</sup> The films were sensitized by immersing the SnO<sub>2</sub>/quartz films in 0.1 mM Ru(II)phos in anhydrous ethanol overnight. To provide relevance to photoelectrochemical processes, the mesoporous

SnO<sub>2</sub> films were studied in the presence of aqueous electrolyte (0.1 M HClO<sub>4</sub>, pH = 1). This was achieved by using a second quartz slide and  $\sim 60$   $\mu\text{m}$  Surllyn spacer (Solaronix) and heating at 250 °C for 45 s to seal them together. The electrolyte was added by vacuum backfilling through a fill hole in the top quartz slide.<sup>15</sup> The fill hole was sealed with a piece of Surllyn and microscope slide coverslip to prevent evaporation and leakage of the solvent.

**Time-Resolved THz Spectroscopy.** Optical pump–THz probe spectroscopy (OPTP) can explore femto- to nanosecond semiconductor carrier dynamics upon photoexcitation.<sup>12,23–27</sup> In this study, an amplified Ti:sapphire laser (Spectra-Physics Spitfire Ace) with a 4 W output of 35 fs pulsed light at a center wavelength of 800 nm and a 1 kHz repetition rate was used. A detailed description of the spectrometer is available elsewhere.<sup>13</sup> Briefly, the output is split into three beams: optical pump excitation, THz probe generation, and THz pulse detection. The THz probe pulse is generated by plasma generation via wave mixing of the fundamental wave and second harmonic in air.<sup>28</sup> The detection beam measures the THz probe by free space electro-optical sampling in a zinc telluride (ZnTe  $\langle 110 \rangle$ ) crystal.<sup>29</sup> In this study, optical excitation of the sample was performed with either the second (400 nm) or the third (267 nm) harmonic of the 800 nm laser output for dye-sensitized and nonsensitized samples, respectively. Generation of second harmonic light was accomplished using a 500  $\mu\text{m}$  thick Type 1  $\beta$ -barium borate crystal (BBO, Eskima Optics). The third harmonic was generated with a Type 1 second harmonic generation (SHG) BBO, a calcite compensation plate (45  $\mu\text{m}$  thick), a  $\lambda/2$  wave plate (for 800 nm), and a Type 1 third harmonic generation (THG) BBO crystal (Newlight Photonics) which are optimized for a 35 fs pulse width.

In the OPTP configuration only the peak amplitude of the THz pulse is measured as a function of  $t_{\text{pump}}$ . Time-dependent changes in the mobile electron population due to trapping or recombination were monitored by using a mechanical delay stage to vary the time between the excitation pulse and THz monitoring pulse. The trapping/recombination dynamics were monitored over an  $\sim 2$  ns time window. The amplitude difference between the photoexcited and nonphotoexcited sample is defined as  $\Delta\text{THz}$ . While these measurements do not present frequency-dependent conductivity information, they provide a spectrally averaged transmission measurement as a function of the pump–probe delay time and therefore can be used to study carrier trapping and recombination dynamics.

The frequency-dependent THz complex photoconductivity was determined by collecting the full transient electric field of the THz pulse at a given time delay after excitation ( $t_{\text{pump}}$ ) and referenced to the THz pulse of the nonphotoexcited material. The measured THz transients at a particular  $t_{\text{pump}}$  are then Fourier transformed, in order to calculate the frequency-dependent conductivity spectrum using the thin-film approximation. In this approximation, any change in transmission between the photoexcited and the nonphotoexcited measurement is attributed to a thin conducting layer of SnO<sub>2</sub>.<sup>23,30</sup> The full THz pulses were each collected over 30 min by averaging 20 individual scans. Full spectral information was collected at five representative pump–probe delays per sample.

## ■ RESULTS AND DISCUSSION

**Pump Fluence Dependence on Direct Band Gap Excitation of SnO<sub>2</sub>.** THz radiation is attenuated by mobile

electrons injected from a sensitizer and by both electrons and holes generated by direct above band gap excitation. The transmission of THz radiation is attenuated in proportion to the conductivity of the sample, which in turn is proportional to the product of carrier density,  $N$ , and mobility,  $\mu$

$$-\Delta\text{THz} \propto N_e \mu_e + N_h \mu_h \quad (1)$$

Both electrons ( $e$ ) and holes ( $h$ ) may contribute. Since the hole effective mass in  $\text{SnO}_2$  is roughly five times greater than that for electrons,<sup>31</sup> the contribution of the holes can be neglected. Additionally,  $\text{SnO}_2$  has a small electron effective mass ( $m^* = 0.275 m_e$ ).<sup>32</sup> Since  $\mu$  is inversely proportional to  $m^*$ , the electron mobility is significantly higher in  $\text{SnO}_2$  compared to other metal oxides such as  $\text{TiO}_2$  ( $m^* = 10 m_e$ )<sup>33</sup> and  $\text{WO}_3$  ( $m^* = 2.4 m_e$ ),<sup>34</sup> and therefore the transmission change upon photoexcitation ( $\Delta\text{THz}$ ) is larger in  $\text{SnO}_2$ .

There has been one previous THz spectroscopic study by Zervos et al. of nonsensitized  $\text{SnO}_2$  nanorods in air excited at 267 nm.<sup>35</sup> Our study differs from their work due to the fact that all of our measurements are made in 60  $\mu\text{m}$  of aqueous electrolyte, and the  $\text{SnO}_2$  nanoparticles themselves are orders of magnitude smaller. While the band gap of  $\text{SnO}_2$  (3.7 eV)<sup>19</sup> is too large to harvest a meaningful portion of the solar spectrum, directly excited  $\text{SnO}_2$  offers a useful point of comparison for dye-sensitized  $\text{SnO}_2$  and can help to establish the underlying material properties relevant to carrier dynamics.

Our previous studies of ultrafast trapping dynamics in mesoporous tungsten(VI) oxide ( $\text{WO}_3$ ) films in an aqueous electrolyte revealed that the photoinduced charge carrier trapping dynamics through above band gap excitation was well described by a stretched exponential function with a long-time offset,  $y_0$ , convoluted with a Gaussian response function ( $G_R$ ) of a particular full-width at half-maximum (fwhm).<sup>13</sup> This model will be used in the present work.

$$-\Delta\text{THz} = \left[ A \exp\left(\left(-\frac{t_{\text{pump}}}{\tau}\right)^\beta\right) + y_0 \right] \otimes G_R(\text{fwhm}) \quad (2)$$

$A$  corresponds to the amplitude of the stretched exponential dynamics;  $\tau$  is the lifetime of the stretched exponential function; and  $\beta$  is the stretching parameter. The  $\beta$  value was fixed at 0.4 for each trace during the nonlinear least-squares fitting procedure. The average lifetime of carriers,  $\langle\tau\rangle$ , is given by the integrated area underneath the stretched exponential curve

$$\langle\tau\rangle = \frac{\tau}{\beta} \Gamma\left(\frac{1}{\beta}\right) \quad (3)$$

where  $\Gamma()$  is the Gamma function.<sup>36</sup> The nonsensitized  $\text{SnO}_2$  films were sealed with an aqueous electrolyte of 0.1 M  $\text{HClO}_4$  (pH = 1), and 267 nm light was used to promote mobile charge carriers into the conduction band. Each of the traces in Figure 1 were taken over an  $\sim 2$  ns time window and were fit with eq 2. The photoexcitation beam is significantly broadened in the time domain due to the unavoidable dispersion in a THG setup. This temporal broadening is accounted for by using an instrument response function fwhm of 1 ps compared to 0.5 ps for excitation at 400 nm.<sup>15</sup>

OPTP traces were taken at pump fluences of  $F = 60, 90, 120,$  and  $155 \mu\text{J}/\text{cm}^2$ . We observed a pump fluence dependence for both the carrier concentration,  $A$  and  $y_0$ , and carrier dynamics,  $\langle\tau\rangle$ . An increase in  $F$  resulted in a linear increase in the

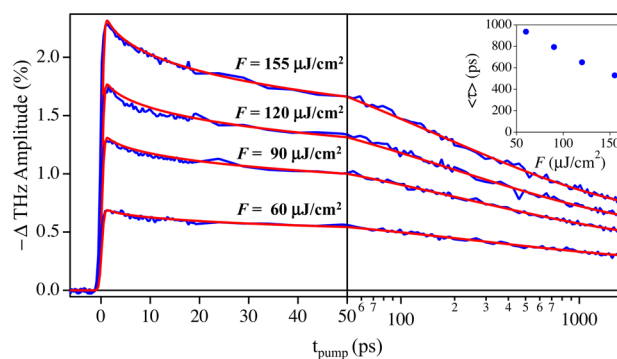


**Figure 1.** OPTP spectroscopy of mesoporous nonsensitized  $\text{SnO}_2$  films immersed in 0.1 M  $\text{HClO}_4$  at pH = 1. The traces were taken at pump fluences of  $F = 60, 90, 120,$  and  $155 \mu\text{J}/\text{cm}^2$  and a wavelength of 267 nm. The red lines represent the best fit of eq 2. The inset depicts the average trapping lifetime,  $\langle\tau\rangle$ , as a function of pump fluence determined by eq 3.

stretched exponential amplitude,  $A$ , and the  $y_0$  offset yet a near-linear decrease in the average lifetime of carriers,  $\langle\tau\rangle$ , determined by eq 3, and is shown in the inset of Figure 1.

The decrease in  $\langle\tau\rangle$  as a function of  $F$  is understood as a consequence of Auger-like recombination processes in  $\text{SnO}_2$ .<sup>37,38</sup> In colloidal semiconductor films, the particle size is sufficiently small that the electron–hole pair samples the entire volume of the particle.  $\text{SnO}_2$  has an absorption coefficient<sup>39</sup> of  $1 \times 10^5 \text{ cm}^{-1}$  at 267 nm (optical skin depth of 100 nm). Over the range of pump fluences used in this study, there are hundreds of photogenerated electron–hole pairs per nanoparticle. Therefore, an Auger-type recombination where one electron–hole pair undergoes recombination and transfers the energy to another electron or hole becomes possible. As pump fluence increases, the probability of generating multiple electron–hole pairs on a single particle increases, thus the observed dependence of  $\langle\tau\rangle$  on fluence. Othonos et al.<sup>40</sup> characterized ultrafast carrier relaxation in  $\text{SnO}_2$  nanowires and found that at pump fluences greater than  $50 \mu\text{J}/\text{cm}^2$  Auger recombination was important. Ford et al.<sup>41</sup> previously analyzed stretched exponential recombination kinetics in dye-sensitized  $\text{SnO}_2$  and found them to be consistent with an Auger-type recombination process. We also note that in addition to Auger recombination trapping and non-Auger recombination are occurring at the same time in a heterogeneous environment, and this complicates the kinetic analysis. We find that all of these recombination mechanisms occurring simultaneously are best described with a stretched-exponential model.

**Pump Fluence Dependence of Dye-Sensitized  $\text{SnO}_2$ .** An alternative strategy to introduce mobile electrons into the conduction band of  $\text{SnO}_2$  is by sensitizing the  $\text{SnO}_2$  film with a visible-light absorbing dye.<sup>9,42,43</sup> In this study, we chose to use a well-studied ruthenium chromophore, Ru(II)phos, which is a derivative of ruthenium(II) trisbipyridine and is anchored to the  $\text{SnO}_2$  by phosphate anchoring groups.<sup>15,44–47</sup> The dye is excited with 400 nm light, and because the excited state energy of the dye is well above that of the  $\text{SnO}_2$  CBM,<sup>42</sup> electrons undergo interfacial electron transfer from the dye. This results in generation of mobile electrons within the metal oxide. Most experimental techniques do not measure these mobile electrons directly.

The majority of ultrafast techniques monitors transient changes in absorption from either the dye radical cation (UV–vis region),<sup>44</sup> intraband transitions (mid-IR region), or trapped

electrons (near-IR region).<sup>47–49</sup> THz transmission measurements, on the other hand, are sensitive to the transient conductivity of the sample, which is directly linked to the density of free carriers. It is a noncontact electrical probe with subpicosecond time resolution and is an excellent method to investigate transient photoconductivity. SnO<sub>2</sub> is an ideal model system due to its band gap energy of 3.7 eV. That is, its band gap is large enough so that we can completely decouple direct band gap excitation from dye-sensitized injection. When exciting nonsensitized SnO<sub>2</sub> films sealed with electrolyte at 400 nm no mobile carriers were generated in the conduction band.<sup>9,15</sup>

The injection dynamics of Ru(II)phos bound to SnO<sub>2</sub> was previously studied at a single pump fluence.<sup>15,47</sup> Here we have examined the OPTP response at four different pump fluences (130, 250, 380, and 510 μJ/cm<sup>2</sup>) to determine the manner in which injection dynamics are influenced (Figure 2). Our

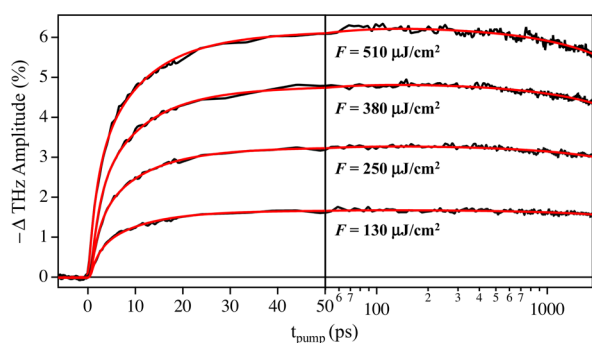


**Figure 2.** OPTP spectroscopy of mesoporous SnO<sub>2</sub> films sensitized with Ru(II)phos dye that are immersed in 0.1 M HClO<sub>4</sub> at pH = 1. The traces were taken with a 400 nm pump wavelength and fluences of 130, 250, 380, and 510 μJ/cm<sup>2</sup>. The red lines represent the best fits using eq 4.

previous studies demonstrated that injection dynamics are well-described as a summation of exponential functions, describing both the injection and recombination dynamics<sup>46</sup>

$$-\Delta\text{THz} = \left[ \sum_{i=1}^n A_i \exp\left(-\frac{t_{\text{pump}}}{\tau_i}\right) - 1 \right] \otimes G_R(\text{fwhm}) \quad (4)$$

where  $n = 4$  is the number of exponential processes. The amplitude,  $A_i$ , for a particular process is positive if charges are being injected ( $A_i$ ) and negative if they are being trapped ( $-A_i$ ).  $\tau_i$  is the lifetime for a particular exponential process,  $i$ . In agreement with our previous work, the electron injection dynamics were modeled using triexponential injection dynamics and previously reported  $\tau$  values ( $\tau_1 = 1.7$  ps,  $\tau_2 = 9.4$  ps, and  $\tau_3 = 37.4$  ps).<sup>15</sup> As seen in the best fits shown in Figure 2, the dynamics are in excellent agreement with previous studies.

Varying the pump fluence demonstrates that there is no influence on the overall electron injection dynamics of Ru(II)phos on SnO<sub>2</sub> with an increased concentration of injected carriers. Injection is a fundamentally second-order process dependent on the concentration of excited sensitizers,  $[\text{Ru}^{2+*}]$ , and conduction band acceptor states,  $[n_{\text{CB}}]$ . The rate of injection is then given by

$$\frac{d[\text{Ru}^{2+*}]}{dt_{\text{pump}}} = -k_{\text{injection}}[\text{Ru}^{2+*}][n_{\text{CB}}] \quad (5)$$

where  $k_{\text{injection}}$  is the second-order rate constant for injection. In the case of injection, the density of conduction band acceptor states is significantly larger than the density of excited sensitizers<sup>50</sup> so the rate equation simplifies to

$$\frac{d[\text{Ru}^{2+*}]}{dt_{\text{pump}}} = -k_{\text{inj}}[\text{Ru}^{2+*}] \quad (6)$$

where  $k_{\text{inj}}$  is defined as

$$k_{\text{inj}} = k_{\text{injection}}[n_{\text{CB}}] \quad (7)$$

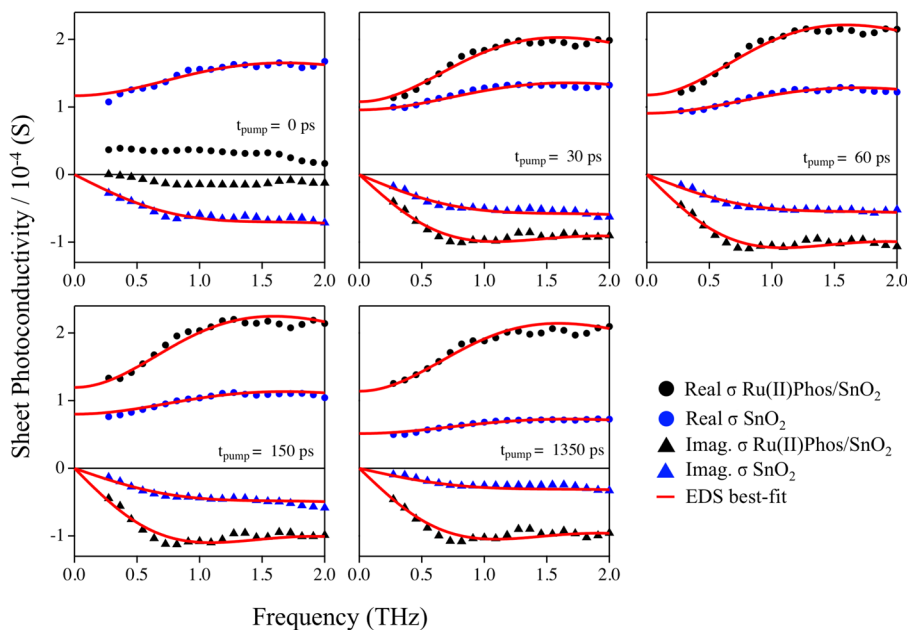


**Figure 3.** Frequency-dependent complex-valued transient sheet photoconductivity measurements were taken at five different  $t_{\text{pump}}$  values, which also correspond to five different areal carrier densities. The measured frequency-dependent conductivity was fit with the EDS model (eq 13).

As a pseudo-first-order process, an increase in the pump fluence will not change the kinetics of injection at a given pH, which is consistent with our results. We previously varied the pH of the electrolyte and demonstrated that the electron injection efficiency and injection rates increase at lower pH values due to a larger driving force for injection.<sup>15</sup>

At longer time scales, we observe recovery of the THz that corresponds to a loss of mobile carriers via a trapping or recombination mechanism. We have previously observed this behavior and suggest that it is related to surface states on the SnO<sub>2</sub> particles.<sup>42</sup> The trapping lifetime,  $\tau_{\text{trap}}$ , of 17 ns was determined by globally fitting a single exponential function simultaneously across all pump fluences. Like injection, trapping is a second-order process dependent on the density of injected electrons in the conduction band and trap states. Because the density of trap states is significantly higher than the density of injected electrons, trapping is also a pseudo-first-order process, and so we would not expect to see a difference in trapping time as a function of fluence.

**Describing the Frequency-Dependent Photoconductivity of SnO<sub>2</sub> Films.** OPTP traces are quite useful for understanding the time scales of injection and trapping/recombination in SnO<sub>2</sub>, yet a fuller understanding of electron dynamics is obtained by probing the frequency-dependent transient photoconductivity at a particular delay time after photoexcitation,  $t_{\text{pump}}$ . Measuring the electric field of the full THz pulse at these delay times allows us to extract the frequency-dependent complex-valued conductivity of the films without any prior assumptions of a conductivity model.

At each  $t_{\text{pump}}$ , the transmitted THz pulse is measured both with and without photoexcitation. The thin-film approximation is used to extract the frequency-dependent photoconductivity.<sup>16</sup> The transient photoconductivity was measured at five  $t_{\text{pump}}$  delays after photoexcitation (0, 30, 60, 150, and 1350 ps; see Figure 3). To allow for a straightforward comparison of the two different samples, pump fluences that resulted in approximately the same maximum value  $\Delta\text{THz}$  were chosen. A pump fluence of 120  $\mu\text{J}/\text{cm}^2$  with 267 nm wavelength was used for the nonsensitized SnO<sub>2</sub> films, and for the dye-sensitized films the pump fluence was 140  $\mu\text{J}/\text{cm}^2$  using a wavelength of 400 nm. The sensitized SnO<sub>2</sub> films differ from the nonsensitized film since the optical penetration depth is roughly 6  $\mu\text{m}$  at 400 nm.

The measurement of the transient complex photoconductivity allows the mobility and carrier density within the CB to be investigated. For bulk crystalline semiconductors, such as silicon (Si) and gallium arsenide (GaAs), photoexcited electrons in the conduction band are well described by the Drude model of conductivity, which treats free electrons as a gas diffusing through the material while undergoing collisions.<sup>24,25,51</sup> The conductivity, denoted  $\hat{\sigma}_{\text{D}}(\omega)$ , is given by<sup>52</sup>

$$\hat{\sigma}_{\text{D}}(\omega) = \frac{Ne^2\tau_{\text{scatt}}/m^*}{1 - i\omega\tau_{\text{scatt}}} \quad (8)$$

where  $N$  is the carrier density;  $e$  is the elementary charge of an electron;  $m^*$  is the effective mass of mobile electrons within the CB of the semiconductor; and  $\omega$  is the angular frequency of the THz probe ( $2\pi\nu_{\text{THz}}$ ). The electron mobility at a given pump delay time,  $\mu_e(t_{\text{pump}})$ , is related to  $\tau_{\text{scatt}}$  and  $m^*$  via:<sup>25</sup>

$$\mu_e(t_{\text{pump}}) = \frac{e\tau_{\text{scatt}}(t_{\text{pump}})}{m^*} \quad (9)$$

Mobility is a measure of how easily charges travel through a material and has a direct influence on THz transmission, as noted in eq 1. The Drude model was developed to describe bulk crystalline materials. Therefore, scattering at surfaces and grain boundaries must be considered when using this model for polycrystalline or mesoporous samples. N. V. Smith found that the Drude model could be improved for disordered materials by including an additional fit parameter,  $c_1$ , which empirically includes the effects of surface and grain boundaries.<sup>20</sup> The resulting Drude–Smith (DS) model is described as<sup>20,26</sup>

$$\hat{\sigma}_{\text{DS}}(\omega) = \frac{Ne^2\tau_{\text{scatt}}/m^*}{1 - i\omega\tau_{\text{scatt}}} \left( 1 + \frac{c_1}{1 - i\omega\tau_{\text{scatt}}} \right) \quad (10)$$

The influence of mobile carriers is the basis of both the Drude model and the DS model. While the DS modification has described the vast majority of experiments on disordered nanostructured materials,<sup>12,13,26,53</sup> it does not satisfactorily agree with our data presented below (see Supporting Information Figure S3). The reason is that contributions from photoexcited localized carriers and/or induced dipoles change the permittivity, which leads to changes in the reported “conductivity”.

Fundamentally, it is impossible to separate the influences of permittivity or conductivity based on the transmission properties of any material by spectroscopic measurements alone. When an electromagnetic wave is transmitted through a material, it is only possible to measure a change in amplitude and a change in phase, which is determined by the generalized permittivity  $\hat{\eta}(\omega)$ . It is well-known that

$$\hat{\eta}(\omega) = \hat{\epsilon}(\omega) + \frac{i\hat{\sigma}(\omega)}{\omega\epsilon_0} \quad (11)$$

where  $\hat{\epsilon}(\omega)$  is the permittivity in the absence of mobile charge carriers, and  $\hat{\sigma}(\omega)$  is the conductivity (which is zero for the nonphotoexcited sample). The permittivity, conductivity, and generalized permittivity are all complex-valued. Therefore, it is seen that while two quantities are measured experimentally to yield the generalized permittivity, there are four quantities embedded in the permittivity and conductivity.

In the case of mesoporous SnO<sub>2</sub> films, we find that the DS model alone is not able to accurately describe the complex transient photoconductivity, and therefore we propose a refined model. If there is a change in the real permittivity upon photoexcitation,  $\Delta\epsilon_{\text{photo}}$ , as a result of charge separation, then it will manifest itself as an apparent change in the imaginary conductivity

$$\hat{\sigma}(\omega) = -i\omega\epsilon_0\Delta\hat{\epsilon}(\omega)_{\text{photo}} \quad (12)$$

where  $\epsilon_0$  is the permittivity of free space and  $\Delta\hat{\epsilon}(\omega)_{\text{photo}}$  is the change in complex permittivity upon photoexcitation. This relation is particularly important because any change in transmission of THz radiation is attributed to a change in the complex transient photoconductivity,  $\hat{\sigma}(\omega)$ . Thus, any change in the permittivity will also be reflected in the transient “conductivity”.

SnO<sub>2</sub> was chosen as a model system to compare how charge generation affects the photoinduced conductivity due to its high mobility of electrons within the CB.<sup>32</sup> Equation 1 indicates the attenuation of THz radiation is directly proportional to carrier density and mobility. Therefore, a large  $\Delta\text{THz}$  can be achieved for a smaller charge carrier density since conductivities in SnO<sub>2</sub> on the order of 20 S/cm are significantly higher than previously

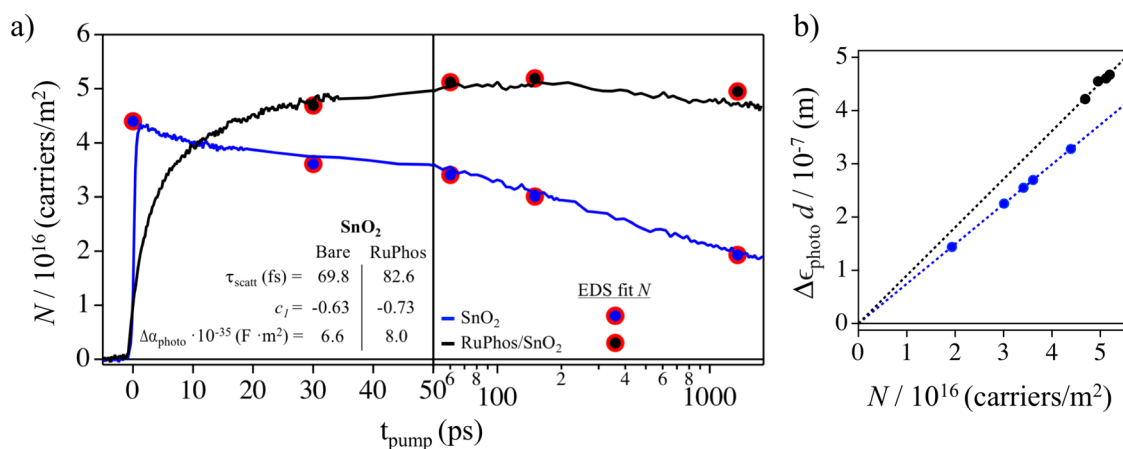


**Figure 4.** (a) Complex transient photoconductivity best-fit parameters are displayed. The total number of carriers,  $N$ , shown as blue and black symbols with red border, was the only parameter varied at each pump–probe delay time. The OPTP traces have been scaled to overlay the carrier density. The values of  $\tau_{\text{scatt}}$ ,  $c_1$ , and  $\Delta\alpha_{\text{photo}}$  are listed for both the nonsensitized and dye-sensitized films. (b)  $\Delta\epsilon_{\text{photo}} \cdot d$  is plotted as a function of the areal carrier density.

reported values for comparable mesoporous metal oxide films, such as TiO<sub>2</sub>, WO<sub>3</sub>, and ZnO.<sup>12,13,26</sup> As a result of a higher signal-to-noise ratio, we identified a contribution to the imaginary conductivity that is not apparent in the lower mobility metal oxides, and this led to the development of the extended EDS model (EDS).

The EDS model accurately describes the frequency-dependent conductivity of the measured samples

$$\hat{\sigma}_{\text{EDS}}(\omega) = \frac{Ne^2\tau_{\text{scatt}}/m^*}{1 - i\omega\tau_{\text{scatt}}} \left( 1 + \frac{c_1}{1 - i\omega\tau_{\text{scatt}}} \right) - i\omega\epsilon_0 \underbrace{\left( \frac{\Delta\alpha_{\text{photo}}N}{\epsilon_0} \right)}_{\Delta\epsilon_{\text{photo}}} \quad (13)$$

where the only modification is the second term on the right that includes a parameter,  $\Delta\alpha_{\text{photo}}$ , which is independent of frequency and carrier density and corresponds to the change in polarizability of the sample upon photoexcitation.

The transient complex photoconductivity data are globally fit, so that the only parameter that is varied at each of the pump–probe delay times,  $t_{\text{pump}}$ , is the carrier density,  $N$ . The other parameters ( $\tau_{\text{scatt}}$ ,  $c_1$ , and  $\Delta\alpha_{\text{photo}}$ ) are material properties that are constant for all pump delays in the fit. Therefore, this model has fewer fit parameters than the DS model but describes the presented data significantly better. Since the skin depth of the nonsensitized and sensitized SnO<sub>2</sub> films is different, we represent the areal density of carriers in the system,  $N/\text{m}^2$ , instead of presenting the carrier density. For the same reason, we present the sheet conductivity (in S) instead of the bulk conductivity in S/cm. Fits of the DS and EDS models are compared in Figure S3 in the Supporting Information. The frequency-dependent transient sheet photoconductivity at each  $t_{\text{pump}}$  is shown in Figure 3 where the red line is the calculated conductivity based on the best-fit parameters of the EDS model.

The EDS model accurately captures the complex photoconductivity data from 0.3 to 2.0 THz. The transient conductivity for the dye-sensitized film at  $t_{\text{pump}} = 0$  ps was not modeled due to the fact that charges are still being injected at that time point. However, the conductivity data are still presented in Figure 3. Figure 4 presents the best-fit parameters from the global fit of the transient conductivity data with eq 13.

A table of the values is found in Table S3 in the Supporting Information.

In addition, the OPTP traces for the nonsensitized and dye-sensitized SnO<sub>2</sub> films taken with the maximum fluence shown in Figures 1 and 2 were scaled and overlaid on the best-fit carrier density values. The  $\tau_{\text{scatt}}$ ,  $c_1$ , and  $\Delta\alpha_{\text{photo}}$  parameters are held constant for all of the delay times during each iteration of the nonlinear least-squares fitting routine and are reported in Figure 4a and Table S3. If  $\Delta\epsilon_{\text{photo}} \cdot d$  (where  $d$  is thickness) is plotted as a function of the total number of carriers, as seen in Figure 4b, the slope ( $\Delta\alpha_{\text{photo}}/\epsilon_0$ ) of this relation yields the change in polarizability of the sample upon photoexcitation,  $\Delta\alpha_{\text{photo}}$ .

This extension to the DS model is based on photogenerated bound charges, which behave as Lorentz oscillators, and has been reported in previous studies.<sup>14,54–56</sup> In a previous study of TiO<sub>2</sub> nanotubes, a clear signature of a resonant Lorentz oscillator was observed within the bandwidth of the conductivity measurements.<sup>14</sup> In the present case, the resonant frequency of the Lorentz oscillator is beyond the bandwidth of these experiments. Therefore, only the low frequency tail of the Lorentz resonance influences our results. The real contribution to this tail is approximately constant, and the imaginary contribution is essentially zero (see Figure S4); this is the origin of the additional constant in the EDS model (eq 13). Similar effects have been reported by Dani and co-workers in hexagonal boron nitride (h-BN).<sup>54</sup>

## CONCLUSIONS

In conclusion, we have utilized OPTP spectroscopy to uncover markedly different carrier dynamics in nonsensitized and dye-sensitized SnO<sub>2</sub> films. Both samples were sealed with an aqueous electrolyte solution to mimic the conditions of a working PEC. It was found that the nonsensitized SnO<sub>2</sub> films exhibited instrument response limited injection dynamics and 2 orders of magnitude faster trapping dynamics compared to the dye-sensitized films. In the nonsensitized films, an increase in the carrier density by increasing the pump fluence caused a decrease in the overall lifetime of mobile carriers, which is consistent with Auger recombination.<sup>37,40,41</sup> The dye-sensitized films required tens of picoseconds for interfacial electron transfer to complete. It was found that the pump fluence had

no influence on the overall injection and trapping dynamics since the density of mobile electrons is far smaller than that of conduction band acceptor states (injection) and the density of trap states (trapping).

In addition, we compared the frequency-dependent complex-valued THz transient photoconductivity of a metal oxide film submerged in aqueous electrolyte solution in which mobile charge carriers are photogenerated by two different methods: direct above-band gap excitation vs interfacial electron transfer from a photoexcited dye sensitizer. Analysis of the complex-valued transient photoconductivity spectra of both the nonsensitized and dye-sensitized films required that the DS model be extended with a term that is due to photogenerated bound charges. We find that the EDS model describes the frequency-dependent photoconductivity significantly better than the DS model for mesoporous nanoparticulate materials. These new results will lead to a wide variety of future experiments that will compare the influence of solvent, pH, pump fluence, and material-dependent quantities in semiconductor nanomaterials.

## ■ ASSOCIATED CONTENT

### Supporting Information

The Supporting Information is available free of charge on the ACS Publications website at DOI: 10.1021/acs.jpcc.7b02318.

Exact fit values used in Figure 1, 2, and 3; Drude-Smith best fit; permittivity of a Lorentzian oscillator (PDF)

## ■ AUTHOR INFORMATION

### Corresponding Author

\*E-mail: charles.schmittenmaer@yale.edu. Phone: (203) 432-5049.

### ORCID

Kevin P. Regan: 0000-0003-3522-092X

John R. Swierk: 0000-0001-5811-7285

### Notes

The authors declare no competing financial interest.

## ■ ACKNOWLEDGMENTS

This work was funded by the U.S. Department of Energy Office of Science, Office of Basic Energy Sciences, under award no. DE-FG02-07ER15909, and by a generous donation from the TomKat Charitable Trust. Jens Neu acknowledges support from the National Science Foundation (NSF CHE-1465085).

## ■ REFERENCES

- (1) Gratzel, M. Photoelectrochemical Cells. *Nature* **2001**, *414*, 338–344.
- (2) Liu, R.; Lin, Y.; Chou, L.-Y.; Sheehan, S. W.; He, W.; Zhang, F.; Hou, H. J. M.; Wang, D. Water Splitting by Tungsten Oxide Prepared by Atomic Layer Deposition and Decorated with an Oxygen-Evolving Catalyst. *Angew. Chem., Int. Ed.* **2011**, *50*, 499–502.
- (3) Brennan, B. J.; Regan, K. P.; Durrell, A. C.; Schmittenmaer, C. A.; Brudvig, G. W. Solvent Dependence of Lateral Charge Transfer in a Porphyrin Monolayer. *ACS Energy Lett.* **2017**, *2*, 168–173.
- (4) Li, J.; Wu, N. Semiconductor-based Photocatalysts and Photoelectrochemical Cells for Solar Fuel Generation: A Review. *Catal. Sci. Technol.* **2015**, *5*, 1360–1384.
- (5) Tachibana, Y.; Vayssieres, L.; Durrant, J. R. Artificial Photosynthesis for Solar Water-Splitting. *Nat. Photonics* **2012**, *6*, 511–518.
- (6) Pesci, F. M.; Cowan, A. J.; Alexander, B. D.; Durrant, J. R.; Klug, D. R. Charge Carrier Dynamics on Mesoporous WO<sub>3</sub> During Water Splitting. *J. Phys. Chem. Lett.* **2011**, *2*, 1900–1903.
- (7) Jensen, S. A.; Tielrooij, K.-J.; Hendry, E.; Bonn, M.; Rychetský, I.; Němec, H. Terahertz Depolarization Effects in Colloidal TiO<sub>2</sub> Films Reveal Particle Morphology. *J. Phys. Chem. C* **2014**, *118*, 1191–1197.
- (8) Nadochenko, V. A.; Denisov, N. N.; Gak, V. Y.; Gostev, F. E.; Titov, A. A.; Sarkisov, O. M.; Nikandrov, V. V. Femtosecond Relaxation of Photoexcited States in Nanosized Semiconductor Particles of Ion Oxides. *Russ. Chem. Bull.* **2002**, *51*, 457–461.
- (9) Milot, R. L.; Moore, G. F.; Crabtree, R. H.; Brudvig, G. W.; Schmittenmaer, C. A. Electron Injection Dynamics from Photoexcited Porphyrin Dyes into SnO<sub>2</sub> and TiO<sub>2</sub> Nanoparticles. *J. Phys. Chem. C* **2013**, *117*, 21662–21670.
- (10) Li, C.; et al. Facet-Dependent Photoelectrochemical Performance of TiO<sub>2</sub> Nanostructures: An Experimental and Computational Study. *J. Am. Chem. Soc.* **2015**, *137*, 1520–1529.
- (11) Swierk, J. R.; Regan, K. P.; Jiang, J.; Brudvig, G. W.; Schmittenmaer, C. A. Rutile TiO<sub>2</sub> as an Anode Material for Water-Splitting Dye-Sensitized Photoelectrochemical Cells. *ACS Energy Lett.* **2016**, *1*, 603–606.
- (12) Baxter, J. B.; Schmittenmaer, C. A. Conductivity of ZnO Nanowires, Nanoparticles, and Thin Films Using Time-Resolved Terahertz Spectroscopy. *J. Phys. Chem. B* **2006**, *110*, 25229–25239.
- (13) Regan, K. P.; Koenigsmann, C.; Sheehan, S. W.; Konezny, S. J.; Schmittenmaer, C. A. Size-Dependent Ultrafast Charge Carrier Dynamics of WO<sub>3</sub> for Photoelectrochemical Cells. *J. Phys. Chem. C* **2016**, *120*, 14926–14933.
- (14) Richter, C.; Schmittenmaer, C. A. Exciton-like Trap States Limit Electron Mobility in TiO<sub>2</sub> Nanotubes. *Nat. Nanotechnol.* **2010**, *5*, 769–772.
- (15) Swierk, J. R.; McCool, N. S.; Nemes, C. T.; Mallouk, T. E.; Schmittenmaer, C. A. Ultrafast Electron Injection Dynamics of Photoanodes for Water-Splitting Dye-Sensitized Photoelectrochemical Cells. *J. Phys. Chem. C* **2016**, *120*, 5940–5948.
- (16) Tiwana, P.; Docampo, P.; Johnston, M. B.; Snaith, H. J.; Herz, L. M. Electron Mobility and Injection Dynamics in Mesoporous ZnO, SnO<sub>2</sub>, and TiO<sub>2</sub> Films Used in Dye-Sensitized Solar Cells. *ACS Nano* **2011**, *5*, 5158–5166.
- (17) Pijpers, J. J. H.; Ulbricht, R.; Derossi, S.; Reek, J. N. H.; Bonn, M. Picosecond Electron Injection Dynamics in Dye-Sensitized Oxides in the Presence of Electrolyte. *J. Phys. Chem. C* **2011**, *115*, 2578–2584.
- (18) Brauer, J. C.; Marchioro, A.; Paraecattil, A. A.; Oskoue, A. A.; Moser, J.-E. Dynamics of Interfacial Charge Transfer States and Carriers Separation in Dye-Sensitized Solar Cells: A Time-Resolved Terahertz Spectroscopy Study. *J. Phys. Chem. C* **2015**, *119*, 26266–26274.
- (19) Bagheri-Mohagheghi, M. M.; Shahtahmasebi, N.; Alinejad, M. R.; Youssefi, A.; Shokooh-Saremi, M. The Effect of the Post-Annealing Temperature on the Nano-Structure and Energy Band Gap of SnO<sub>2</sub> Semiconducting Oxide Nano-Particles Synthesized by Polymerizing–Complexing Sol–Gel Method. *Phys. B* **2008**, *403*, 2431–2437.
- (20) Smith, N. V. Classical Generalization of the Drude Formula for the Optical Conductivity. *Phys. Rev. B: Condens. Matter Mater. Phys.* **2001**, *64*, 155106.
- (21) Ito, S.; Chen, P.; Comte, P.; Nazeeruddin, M. K.; Liska, P.; Péchy, P.; Grätzel, M. Fabrication of Screen-Printing Pastes from TiO<sub>2</sub> Powders for Dye-Sensitized Solar Cells. *Prog. Photovoltaics* **2007**, *15*, 603–612.
- (22) Gillaizeau-Gauthier, I.; Odobel, F.; Alebbi, M.; Argazzi, R.; Costa, E.; Bignozzi, C. A.; Qu, P.; Meyer, G. J. Phosphonate-Based Bipyridine Dyes for Stable Photovoltaic Devices. *Inorg. Chem.* **2001**, *40*, 6073–6079.
- (23) Jepsen, P. U.; Cooke, D. G.; Koch, M. Terahertz Spectroscopy and Imaging – Modern Techniques and Applications. *Laser Photon. Rev.* **2011**, *5*, 124–166.
- (24) Beard, M. C.; Turner, G. M.; Schmittenmaer, C. A. Terahertz Spectroscopy. *J. Phys. Chem. B* **2002**, *106*, 7146–7159.
- (25) Beard, M. C.; Turner, G. M.; Schmittenmaer, C. A. Transient Photoconductivity in GaAs as Measured by Time-Resolved Terahertz Spectroscopy. *Phys. Rev. B: Condens. Matter Mater. Phys.* **2000**, *62*, 15764–15777.

- (26) Turner, G. M.; Beard, M. C.; Schmittenmaer, C. A. Carrier Localization and Cooling in Dye-Sensitized Nanocrystalline Titanium Dioxide. *J. Phys. Chem. B* **2002**, *106*, 11716–11719.
- (27) Neu, J.; Rahm, M. Terahertz Time Domain Spectroscopy for Carrier Lifetime Mapping in the Picosecond to Microsecond Regime. *Opt. Express* **2015**, *23*, 12900–12909.
- (28) Kress, M.; Löffler, T.; Eden, S.; Thomson, M.; Roskos, H. G. Terahertz-Pulse Generation by Photoionization of Air with Laser Pulses Composed of Both Fundamental and Second-Harmonic Waves. *Opt. Lett.* **2004**, *29*, 1120–1122.
- (29) Wu, Q.; Zhang, X. C. Freespace Electrooptic Sampling of Terahertz Beams. *Appl. Phys. Lett.* **1995**, *67*, 3523–3525.
- (30) Tinkham, M. Energy Gap Interpretation of Experiments on Infrared Transmission through Superconducting Films. *Phys. Rev.* **1956**, *104*, 845–846.
- (31) Schleife, A.; Varley, J. B.; Fuchs, F.; Rödl, C.; Bechstedt, F.; Rinke, P.; Janotti, A.; Van de Walle, C. G. Tin Dioxide from First Principles: Quasiparticle Electronic States and Optical Properties. *Phys. Rev. B: Condens. Matter Mater. Phys.* **2011**, *83*, 035116.
- (32) Button, K. J.; Fonstad, C. G.; Dreybrodt, W. Determination of the Electron Masses in Stannic Oxide by Submillimeter Cyclotron Resonance. *Phys. Rev. B* **1971**, *4*, 4539–4542.
- (33) Goodenough, J. B. H. A. *Semiconductors, Group III: Crystal and Solid State Physics*; Springer-Verlag: Berlin, 1984; Vol. 17g.
- (34) Chen, R. S.; Wang, W. C.; Lu, M. L.; Chen, Y. F.; Lin, H. C.; Chen, K. H.; Chen, L. C. Anomalous Quantum Efficiency for Photoconduction and its Power Dependence in Metal Oxide Semiconductor Nanowires. *Nanoscale* **2013**, *5*, 6867–6873.
- (35) Tsokkou, D.; Othonos, A.; Zervos, M. Carrier Dynamics and Conductivity of SnO<sub>2</sub> Nanowires Investigated by Time-Resolved Terahertz Spectroscopy. *Appl. Phys. Lett.* **2012**, *100*, 133101.
- (36) Laherrère, J.; Sornette, D. Stretched Exponential Distributions in Nature and Economy: “Fat Tails” with Characteristic Scales. *Eur. Phys. J. B* **1998**, *2*, 525–539.
- (37) Landsberg, P. T. Trap Auger Recombination in Silicon of Low Carrier Densities. *Appl. Phys. Lett.* **1987**, *50*, 745–747.
- (38) Weller, H. Quantized Semiconductor Particles: A Novel State of Matter for Materials Science. *Adv. Mater.* **1993**, *5*, 88–95.
- (39) Chowdhury, F. R.; Choudhury, S.; Hasan, F.; Begum, T. Optical Properties of Undoped and Indium-doped Tin Oxide Thin Films. *J. Bangladesh Acad. Sci.* **2011**, *35*, 13.
- (40) Othonos, A.; Zervos, M.; Tsokkou, D. Tin Oxide Nanowires: The Influence of Trap States on Ultrafast Carrier Relaxation. *Nanoscale Res. Lett.* **2009**, *4*, 828.
- (41) Ford, W. E.; Wessels, J. M.; Rodgers, M. A. J. Electron Injection by Photoexcited Ru(bpy)<sub>3</sub><sup>2+</sup> into Colloidal SnO<sub>2</sub>: Analyses of the Recombination Kinetics Based on Electrochemical and Auger-Capture Models. *J. Phys. Chem. B* **1997**, *101*, 7435–7442.
- (42) McCool, N. S.; Swierk, J. R.; Nemes, C. T.; Schmittenmaer, C. A.; Mallouk, T. E. Dynamics of Electron Injection in SnO<sub>2</sub>/TiO<sub>2</sub> Core/Shell Electrodes for Water-Splitting Dye-Sensitized Photoelectrochemical Cells. *J. Phys. Chem. Lett.* **2016**, *7*, 2930–2934.
- (43) Wee, K.-R.; Sherman, B. D.; Brennaman, M. K.; Sheridan, M. V.; Nayak, A.; Alibabaei, L.; Meyer, T. J. An Aqueous, Organic Dye Derivatized SnO<sub>2</sub>/TiO<sub>2</sub> Core/shell Photoanode. *J. Mater. Chem. A* **2016**, *4*, 2969–2975.
- (44) Giokas, P. G.; Miller, S. A.; Hanson, K.; Norris, M. R.; Glasson, C. R. K.; Concepcion, J. J.; Bettis, S. E.; Meyer, T. J.; Moran, A. M. Spectroscopy and Dynamics of Phosphonate-Derivatized Ruthenium Complexes on TiO<sub>2</sub>. *J. Phys. Chem. C* **2013**, *117*, 812–824.
- (45) Hanson, K.; et al. Structure–Property Relationships in Phosphonate-Derivatized, RuII Polypyridyl Dyes on Metal Oxide Surfaces in an Aqueous Environment. *J. Phys. Chem. C* **2012**, *116*, 14837–14847.
- (46) Swierk, J. R.; McCool, N. S.; Mallouk, T. E. Dynamics of Electron Recombination and Transport in Water-Splitting Dye-Sensitized Photoanodes. *J. Phys. Chem. C* **2015**, *119*, 13858–13867.
- (47) Xiang, X.; Fielden, J.; Rodríguez-Córdoba, W.; Huang, Z.; Zhang, N.; Luo, Z.; Musaev, D. G.; Lian, T.; Hill, C. L. Electron Transfer Dynamics in Semiconductor–Chromophore–Polyoxometalate Catalyst Photoanodes. *J. Phys. Chem. C* **2013**, *117*, 918–926.
- (48) Asbury, J. B.; Hao, E.; Wang, Y.; Ghosh, H. N.; Lian, T. Ultrafast Electron Transfer Dynamics from Molecular Adsorbates to Semiconductor Nanocrystalline Thin Films. *J. Phys. Chem. B* **2001**, *105*, 4545–4557.
- (49) Furube, A.; Tamaki, Y.; Murai, M.; Hara, K.; Katoh, R.; Tachiya, M. *Proc. SPIE 6643, Physical Chemistry of Interfaces and Nanomaterials VI*, art. no. 66430J, 2007, DOI: [10.1117/12.733316](https://doi.org/10.1117/12.733316).
- (50) Vohs, J. M. *The Surface Science of Metal Oxides*; Wiley Subscription Services, Inc., A Wiley Company: Cambridge, U.K., 1998; Vol. 44, pp 502–503.
- (51) Exter, M. v.; Grischkowsky, D. Optical and Electronic Properties of Doped Silicon from 0.1 to 2 THz. *Appl. Phys. Lett.* **1990**, *56*, 1694–1696.
- (52) G.Grüner, M. D. *Electrodynamics of Solids: Optical Properties of Electrons in Matter*; Cambridge University Press: Cambridge, UK, 2002.
- (53) Lloyd-Hughes, J.; Jeon, T.-I. A Review of the Terahertz Conductivity of Bulk and Nano-Materials. *J. Infrared, Millimeter, Terahertz Waves* **2012**, *33*, 871–925.
- (54) Krishna, M. B. M.; et al. Engineering Photophenomena in Large, 3D Structures Composed of Self-Assembled van der Waals Heterostructure Flakes. *Adv. Opt. Mater.* **2015**, *3*, 1551–1556.
- (55) Zajac, V.; Němec, H.; Kužel, P. Picosecond Charge Transport in Rutile at High Carrier Densities Studied by Transient Terahertz Spectroscopy. *Phys. Rev. B: Condens. Matter Mater. Phys.* **2016**, *94*, 115206.
- (56) Wang, F.; Shan, J.; Islam, M. A.; Herman, I. P.; Bonn, M.; Heinz, T. F. Exciton Polarizability in Semiconductor Nanocrystals. *Nat. Mater.* **2006**, *5*, 861–864.

## Supporting Information

Frequency-Dependent Terahertz Transient Photoconductivity of Mesoporous SnO<sub>2</sub> Films

*Kevin P. Regan<sup>1,2</sup>, John R. Swierk<sup>1,2</sup>, Jens Neu<sup>1</sup>, and Charles A. Schmuttenmaer<sup>1,2\*</sup>*

<sup>1</sup>Department of Chemistry, and <sup>2</sup>Yale Energy Sciences Institute, Yale University, New Haven, CT  
06520-8107, United States

\*Email: [charles.schmuttenmaer@yale.edu](mailto:charles.schmuttenmaer@yale.edu), (203) 432-5049

### Contents:

1) Best-fit parameters of Equation 2 to non-sensitized SnO <sub>2</sub> films sealed in aqueous electrolyte....	S2
2) Best-fit parameters of Equation 4 to dye-sensitized SnO <sub>2</sub> films sealed in aqueous electrolyte....	S3
3) Comparison of Drude-Smith Model and Extended Drude-Smith Model.....	S4
4) Best-fit parameters of Equation 13 for the transient photoconductivity. ....	S5
4) Lorentz Oscillator.....	S6

### 1) Best-fit parameters of Equation 2 to non-sensitized SnO<sub>2</sub> films sealed in aqueous electrolyte.

**Table S1:** Best-fit parameters of equation 2 from non-sensitized SnO<sub>2</sub> films photoexcited with 267 nm light. The pump fluence was varied from 60, 90, 120, and 155  $\mu\text{J}/\text{cm}^2$ .

$F$ ( $\mu\text{J}/\text{cm}^2$ )	fwhm (ps)	$A$ (%)	$\beta$	$\tau$ (ps)	$\langle\tau\rangle$ (ps)	$y_o$ (%)
60	1	0.51	0.4	282.0	937	0.24
90	1	1.10	0.4	238.8	794	0.40
120	1	1.43	0.4	196.3	652	0.52
155	1	1.95	0.4	159.8	530	0.62

Table S1 presents the best-fit parameters obtained from fitting the non-sensitized SnO<sub>2</sub> films at four different pump fluences in the presence of aqueous electrolyte. Figure S1 depicts the linear dependence of both  $A$  and  $y_o$  as a function of pump fluence.

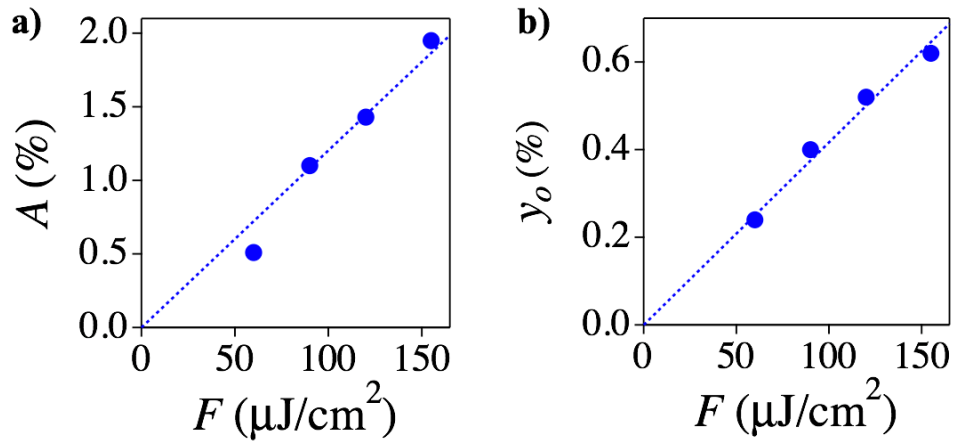


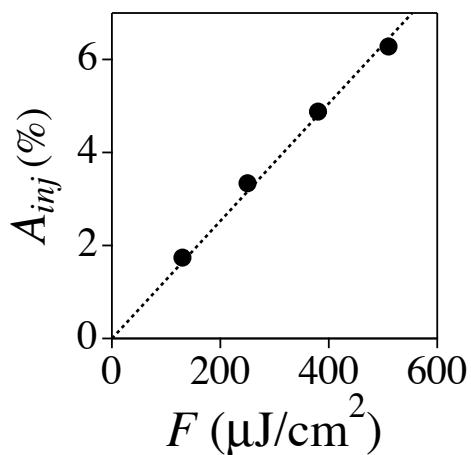
**Figure S1:** a) Plot of the amplitude of the stretched exponential function,  $A$ , as a function of pump fluence. b) Plot of the long-time offset,  $y_o$ , as a function of pump fluence. The dotted lines represent the best linear fit, and is constrained to pass through the origin.

## 2) Best-fit parameters of Equation 4 to dye-sensitized SnO<sub>2</sub> films sealed in aqueous electrolyte.

**Table S2:** Best-fit parameters of equation 4 from dye-sensitized SnO<sub>2</sub> films photoexcited with 400 nm light. The pump fluence was varied from 130, 250, 380, and 510  $\mu\text{J}/\text{cm}^2$ .  $A_{inj}$  is simply the sum of  $A_1$ ,  $A_2$ , and  $A_3$ .

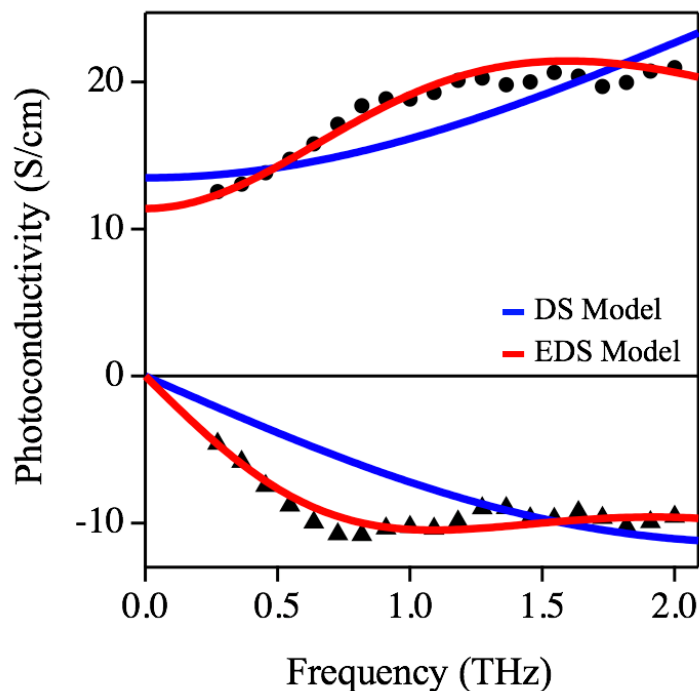
$F$ ( $\mu\text{J}/\text{cm}^2$ )	fwhm (ps)	$A_1$ (%)	$A_2$ (%)	$A_3$ (%)	$A_{inj}$ (%), $-A_{trap}$ (%)	$\tau_{trap}$ (ns)
130	0.5	0.68	0.88	0.18	1.74	17.0
250	0.5	1.35	1.67	0.32	3.34	17.0
380	0.5	1.91	2.60	0.37	4.88	17.0
510	0.5	2.39	3.40	0.49	6.28	17.0

Table S2 reports the best-fit parameters obtained from fitting Equation 4 to the dye-sensitized SnO<sub>2</sub> films sealed in electrolyte. The amplitude of trapping,  $A_{trap}$ , is equal to  $-A_{inj}$ . Figure S2 depicts the linear dependence of injection amplitude on pump fluence.



**Figure S2:** Plot of the total amplitude of injection,  $A_{inj}$ , as a function of pump fluence. The dotted line represents the best linear fit, and is constrained to pass through the origin.

### 3) Comparison of Drude-Smith Model and Extended Drude-Smith Model.



**Figure S3:** Transient photoconductivity measurements taken at  $t_{\text{pump}} = 1350$  ps. The red lines display the best-fit values for the EDS model, and the blue are for the DS Model.

The best-fit results of the DS Model are compared to that of the EDS Model in Figure S3. It is clear that the EDS Model more accurately represents the frequency domain data. Note in particular that the EDS Model reproduces the low frequency imaginary conductivity significantly better.

#### 4) Best-fit parameters of Equation 13 for the transient photoconductivity.

**Table S3:** Best-fit parameters from the global fit of Equation 13.

	<b>SnO<sub>2</sub></b>	<b>Ru(II)phos / SnO<sub>2</sub></b>
$t_{\text{pump}}$ (ps) =	$N \text{ (cm}^{-3}\text{) } / 10^{17}$	$N \text{ (cm}^{-3}\text{) } / 10^{15}$
0	4.40	-
30	3.61	7.81
60	3.41	8.52
150	3.01	8.65
1350	1.93	8.25
$\tau_{\text{scatt}}$ (fs) =	69.8	82.6
$c_I$ =	-0.63	-0.73
$\Delta\alpha_{\text{photo}}$ (F m <sup>2</sup> ) / 10 <sup>-35</sup> =	6.6	8.0

The best-fit parameters from Equation 13 are presented in Table S3. These values were globally fit such that the  $\tau_{\text{scatt}}$ ,  $c_I$ , and  $\Delta\alpha_{\text{photo}}$  are constant across all  $t_{\text{pump}}$ . The only parameter that was allowed to vary at each  $t_{\text{pump}}$  is the carrier density,  $N$ .

#### 4) Lorentz Oscillator.

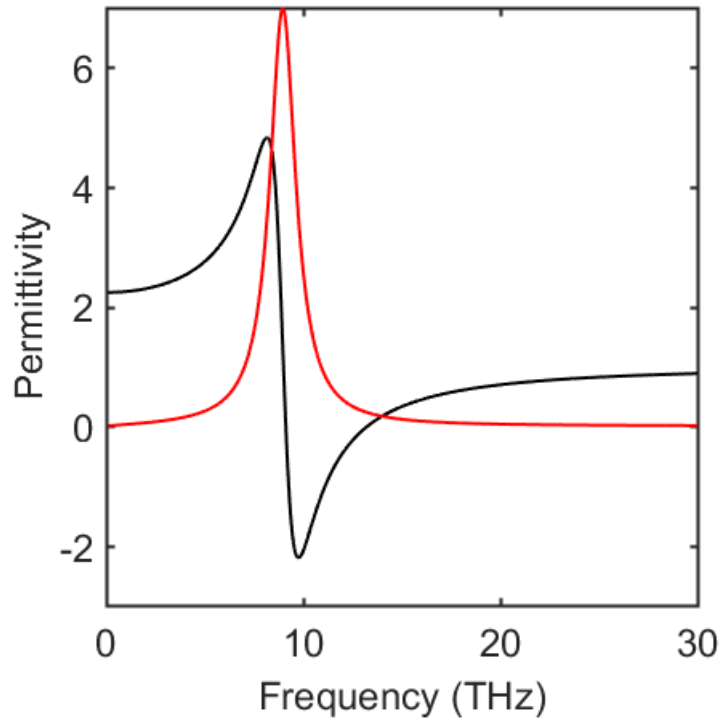


**Figure S4:** A plot of a complex permittivity of a Lorentzian oscillator with a resonance at 9 THz. The black line represents the real portion and the red the imaginary portion of the permittivity.

A change in the real part of the refractive index affects the imaginary part of the conductivity. As seen in figure S4, the real part of the permittivity is nearly constant at frequencies well below the resonance frequency, and the imaginary part is essentially zero. From figure S4, it is clear that before the resonance feature there only exists a significant contribution from the real permittivity, which in turn correlates to the imaginary conductivity.